

## Article

# Correlation Between Morphology and Crystal Structure of Electrolytically Produced Zinc Dendritic Particles

Nebojša D. Nikolić<sup>1,\*</sup>, Jelena D. Lović<sup>1</sup>, Vesna M. Maksimović<sup>2</sup>, Nikola S. Vuković<sup>3</sup>, Nenad L. Ignjatović<sup>4</sup>, Predrag M. Živković<sup>5</sup> and Sanja I. Stevanović<sup>1</sup>

<sup>1</sup> Department of Electrochemistry, Institute of Chemistry, Technology and Metallurgy, University of Belgrade, Njegoševa 12, 11000 Belgrade, Serbia; jelena.lovic@ihmtm.bg.ac.rs (J.D.L.); sanjas@ihmtm.bg.ac.rs (S.I.S.)

<sup>2</sup> Vinča Institute of Nuclear Science—National Institute of the Republic of Serbia, University of Belgrade, Mike Petrovića Alasa 12–14, 11000 Belgrade, Serbia; vesnam@vin.bg.ac.rs

<sup>3</sup> Institute for Technology of Nuclear and Other Mineral Raw Materials, Bulevar Franše d’Eperea 86, 11000 Belgrade, Serbia; n.vukovic@itnms.ac.rs

<sup>4</sup> Institute of Technical Sciences of the Serbian Academy of Science and Arts, Knez Mihailova 35/IV, 11000 Belgrade, Serbia; nenad.ignjatovic@itn.sanu.ac.rs

<sup>5</sup> Faculty of Technology and Metallurgy, University of Belgrade, Karnegijeva 4, 11000 Belgrade, Serbia; peca@tmf.bg.ac.rs

\* Correspondence: nnikolic@ihmtm.bg.ac.rs; Tel.: +381-11-337-0390

**Abstract:** The correlation between the morphology and crystal structure of zinc dendritic particles produced by electrolysis from the alkaline electrolyte has been established. Morphology and crystal structure of Zn particles electrodeposited by the potentiostatic regime of electrolysis at overpotentials inside (−100 and −160 mV) and outside (−220, −280, and −340 mV) the plateau of the limiting diffusion current density were characterized by scanning electron microscope (SEM) and by X-ray diffraction (XRD), respectively. The particle size distribution (PSD) was performed in order to determine the dependency of the size of dendritic particles on applied electrolysis overpotential. With increasing the overpotential of electrolysis, the shape of particles changed from irregular forms denoted as precursors of dendrites to various forms of dendrites, while the size of the particles simultaneously decreased. All types of Zn dendrites exhibited the strong (002) preferred orientation, while the precursors of dendrites exhibited (101)(002) preferred orientation. The development of strong (002) preferred orientation was explained and discussed by making an analogy with the electrolytic production of lead dendrites from the concentrated nitrate electrolyte. Although zinc and lead belong to different types of crystal lattice (Pb-face-centered cubic type and Zn-hexagonal close-packed type), they have a common characteristic that is manifested by the strong preferred orientation in the crystal plane with the lowest surface energy.

**Keywords:** zinc; electrolysis; dendrites; morphology; structure; SEM; XRD; PSD



**Citation:** Nikolić, N.D.; Lović, J.D.; Maksimović, V.M.; Vuković, N.S.; Ignjatović, N.L.; Živković, P.M.; Stevanović, S.I. Correlation Between Morphology and Crystal Structure of Electrolytically Produced Zinc Dendritic Particles. *Metals* **2024**, *14*, 1468. <https://doi.org/10.3390/met14121468>

Academic Editor: Mosab Kaseem

Received: 12 November 2024

Revised: 18 December 2024

Accepted: 20 December 2024

Published: 23 December 2024



**Copyright:** © 2024 by the authors. Licensee MDPI, Basel, Switzerland. This article is an open access article distributed under the terms and conditions of the Creative Commons Attribution (CC BY) license (<https://creativecommons.org/licenses/by/4.0/>).

## 1. Introduction

Zn is a metal that has attracted huge attention from both academic and technological communities for a long time due to its high availability, low price and toxicity, environmental acceptability, and high specific energy [1–3]. Also, Zn possesses high electrical conductivity and chemical stability in various aqueous electrolytes and has good electrochemical reversibility (−0.762 V relative to the standard hydrogen electrode (SHE)). Thanks to all these properties, it is widely used in the production of Zn-based rechargeable batteries, such as zinc–air, zinc–ion batteries, Zn–Ni batteries, and Zn–MnO<sub>2</sub> batteries [2,4,5]. This battery type belongs to a group of green and sustainable energy storage systems and simultaneously represents an excellent replacement for lithium–ion batteries. The morphology of Zn electrodes strongly affects the electrochemical performance of the Zn-based rechargeable batteries. For example, in Zn–MnO<sub>2</sub> batteries, the discharge capacity

of  $220 \text{ mAhg}^{-1}$  is delivered by porous Zn electrodes while only a discharge capacity of  $130 \text{ mAhg}^{-1}$  was delivered by planar Zn electrodes [4]. This increase of 40% can largely be attributed to the porosity of the Zn anode and the subsequent increased surface area of the active metal. Namely, while zincate ions and ZnO products were found after the discharge at the surface of the planar anode, these products were not found in the porous anode, pointing out that the porosity prevents the detrimental buildup of zincate ions at the anodic surface that leads to passivation. Also, Zn is successfully used as a catalyst to electrochemically reduce  $\text{CO}_2$  to CO [6].

The origin of the term “dendrite” is the Greek word *dendron*, which means a tree [3]. The classical definition of a dendrite is given by Wranglen [7], who defined a dendrite as a skeleton of a monocrystal that consists of a stalk and branches. The branches developed from the stalk are marked as primary (P) branches, while those developed from the P branches are marked as secondary (S) branches. If a stalk and branches are in the same plane, then a dendrite is marked as a 2D (two-dimensional) dendrite. If branches grow from a stalk in all directions, then the dendrite is marked as a 3D (three-dimensional) dendrite. The 2D dendrites with P branches, as well as those with P and S branches, are often marked as the fern-like dendrites [8]. The dendrites without branches with the sharp tips are known as the needle-like dendrites [8,9]. The dendrites belong to the group of powdered (dispersed and irregular) deposits and are formed during the diffusion control of electrodeposition [10].

Zinc dendrites can be obtained by the electrochemical deposition (ED) technique from alkaline [1,2,9–18], neutral [17,19,20], and acid [21–23] electrolytes. The other morphological forms that are formed by Zn electrolysis are spongy (mossy), boulders, and different grains of regular and irregular shapes [11,18,24,25]. All relevant parameters of electrolysis affecting the morphology of electrodeposited metals, such as electrolyte pH value, additives, current density, overpotential, temperature, etc., also affect Zn dendrite formation [2]. The electrolytic formation of Zn dendrites has both positive and negative sides. In secondary Zn–air batteries, the growth of Zn dendrites during the charging process can negatively affect the cycle life of the battery by penetrating the separator with sharp tips and by making a short circuit between the anode and the cathode [2,9,26]. In this way, the cycle life of a battery is shortened. Also, Zn dendrites as a type of powdered form, have a weak adhesion, and their spontaneous detachment from the electrode surface causes a loss of battery capacity. For that reason, the effort is also given on an inhibition of dendritic growth of zinc [2,27–29]. The most common way of inhibiting dendritic growth is the introduction of various compounds in zinc electrolytes, such as polymers, organic molecules, and metal ions [2,27,28]. The typical polymers added into electrolytes are polyethylenimine (PEI), Triton X-100, polyethylene glycol (PEG), polyvinyl alcohol (PVA), etc. [27]. Organic compounds, such as 4-aminomethyl cyclohexanecarboxylic acid (AMCA) [28] and many other compounds based on alcohols, aldehydes, organic acids, ammonium compounds, carbohydrates, and surfactants, are widely used for the inhibition of dendritic growth [27]. Finally, metal ions with more positive electrode potentials than zinc, such as bismuth ions ( $\text{Bi}^{3+}$ ) and lead ions ( $\text{Pb}^{2+}$ ), are also used for these purposes. The dendritic growth can be prevented by making a hybrid interface by which direct Zn– $\text{H}_2\text{O}$  contact is fully avoided. It is the case in aqueous calcium ion batteries where an interphase layer with densely packed nanocrystals of  $\text{Ca}_3(\text{CO}_3)_2(\text{OH})_2 \cdot 1.5 \text{ H}_2\text{O}$  and  $\text{ZnF}_2$  and amorphous organic species is demonstrated for a Zn metal anode with 1 M calcium trifluoromethyl sulfonate aqueous electrolyte [29]. The positive side of Zn dendrites is perceived through their use as catalysts for  $\text{CO}_2$  conversion to CO [6]. Thanks to the very high specific surface area caused by branched morphology, Zn dendrites can show an order of magnitude higher activity and three-fold higher faradaic efficiency than bulk Zn [6].

These actual technologies are a cause of numerous and permanent investigations related to the formation and growth of dendrites [30–39]. Despite these investigations, there are still unknowns related to this topic. In the existing investigations, authors usually consider the formation and growth of dendrites, but without a detailed analysis of specific forms of dendrites that can be formed. Also, available information about the crystal structure of Zn dendrites is rare and unsystematic. For that reason, to complete existing knowledge, this study aimed to identify all possible shapes of Zn dendrites that can be obtained under various electrolysis conditions from the alkaline electrolyte and then to correlate the obtained morphology of Zn with their crystal structure.

## 2. Materials and Methods

Zinc was electrodeposited potentiostatically from the alkaline electrolyte at a temperature of  $22.0 \pm 0.50$  °C in an electrochemical cell of a cylindrical shape. Electrodeposition was performed using a potentiostat/galvanostat BioLogic SP 200 (Seyssinet-Pariset, France) at overpotentials of  $-100$ ,  $-160$ ,  $-220$ ,  $-280$ , and  $-340$  mV. The composition of the electrolyte was  $0.35$  M ZnO in  $6.0$  M KOH. This composition was selected because these concentrations of ZnO and KOH, as well as their ratio, represent the typical values used in the Zn–air batteries. For the preparation of the electrolyte, double distilled water (Millipore, 18 M ohm cm resistivity; Merck KGaA, Darmstadt, Germany) and analytical grade reagents supplied by Sigma-Aldrich Company (Sigma-Aldrich, Burlington, MA, USA) were used.

The working electrode (WE) used for ED of Zn was of copper, while the counter (CE) and the reference (RefE) electrodes were of zinc. A Cu WE was cylindrical in shape (length:  $2.0$  cm; diameter:  $0.080$  cm) with an overall surface area of  $0.50$  cm<sup>2</sup> situated in the center of an electrochemical cell. The Zn CE was positioned about the wall of the electrochemical cell, while the tip of the reference electrode was positioned about  $2$  mm from the surface area of the Cu WE.

The cathodic polarization curve was recorded by the linear sweep voltammetry technique using the same WE, RefE, and CE electrodes as those used for Zn electrodeposition at selected overpotentials. A sweep rate of  $1$  mVs<sup>-1</sup> was used during the recording of the polarization curve. All overpotentials are given relative to Zn reference electrode. For this electrodeposition system, Open Circuit Potential (OCP) was  $912 \pm 1.0$  mV vs. Zn.

The preparation of Cu WE for the ED process takes place in several steps: (a) alkaline degreasing at a temperature of  $70$  °C; (b) rinsing in distilled water; (c) acid etching in  $20\%$  H<sub>2</sub>SO<sub>4</sub> at  $50$  °C; and (d) rinsing in distilled water.

### *Characterization of Potentiostatically Produced Zn Dendritic Particles*

Characterization of potentiostatically electrodeposited Zn particles was performed by techniques of scanning electron microscopy (SEM), X-ray diffraction (XRD), and particle size distribution (PSD). The following analyses were performed:

- (a) *Morphology analysis*: Morphological analysis of potentiostatically electrodeposited Zn particles was performed by scanning electron microscope (SEM; model JEOL JSM-7001F JEOL Ltd., Tokyo, Japan). For morphological analysis, ED of Zn was performed with electrodeposited charges of  $0.75$ ,  $1.5$ ,  $3.0$ , and  $6.0$  mAh, and Zn particles were characterized without their removal from the electrode surface after the finished ED process.
- (b) *Structural analysis*: Structural characterization of potentiostatically electrodeposited Zn particles was performed by X-ray diffraction (XRD; Rigaku Ultima IV diffractometer, Rigaku Co., Ltd., Tokyo, Japan). Six reflections in a  $2\theta$  range between  $30$  and  $75^\circ$  were recorded by this diffractometer with CuK $\alpha$  radiation to determine the preferred orientation of produced particles.
- (c) *Analysis of the particle size*: The particle size distribution (PSD) of Zn particles was performed using the MALVERN Instruments MASTERSIZER 2000 device (MALVERN Instruments Ltd., Malvern, Worcestershire, UK).

For XRD and PSD analyses, electrodeposition of Zn was performed with an electrodeposited charge of 18.0 mAh. For these analyses, Zn particles were removed from the Cu WE after the completion of the electrolysis process. The electrolysis process was repeated multiple times to collect enough particles for the analysis. The same amounts of Zn particles were produced at all five overpotentials.

### 3. Results

#### 3.1. Electrochemical Aspects of Electrolytic Production of Zn Dendritic Particles

The cathodic polarization curve for the ED process of Zn from an alkaline electrolyte containing 0.35 M ZnO in 6.0 M KOH is presented in Figure 1. The plateau of the limiting diffusion current density corresponds to an overpotential range between  $-90$  and  $-180$  mV, and the end of the plateau is marked by the beginning of the fast growth of the current density with the increase of overpotential. The electrolytic production of Zn in the form of dendrites commences within the plateau of the limiting diffusion current density, i.e., in the diffusion control of the electrodeposition, and continues to occur in a region of the fast growth of the current density after the inflection point at the polarization curve that denotes the end of the plateau.

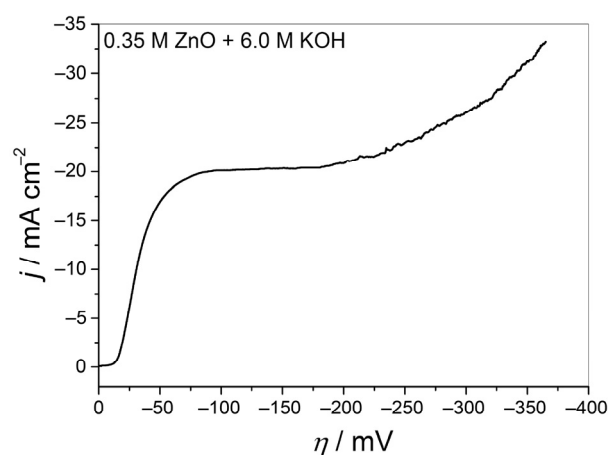


**Figure 1.** The cathodic polarization curve for electrodeposition of Zn from 0.35 M ZnO in 6.0 M KOH. Sweep rate:  $v = 1 \text{ mVs}^{-1}$ .

The chronoamperometry curves recorded at overpotentials of  $-100$  and  $-160$  (the plateau of the limiting diffusion current density),  $-220$ ,  $-280$ , and  $-340$  mV (the zone of the fast increase of the current density with the increasing overpotential) are presented in Figure 2. The common feature of all chronoamperometric curves is a rise in the current density after a certain critical time, with a tendency to shorten this time with increasing the overpotential. The beginning of the growth of the current density coincides with an initiation of dendritic growth [40]. Namely, a growth of dendrites causes a considerable increase of the cathode surface during the electrolysis process [41]. In a potentiostatic regime of electrolysis, since the real current density stays constant during the electrolysis duration, while the cathode surface area increases with time, the final result is an increase of the current density with the electrolysis time in the chronoamperometry curves. According to recorded chronoamperometry curves, the growth of dendrites commences approximately after 810 s at  $-100$  mV, 550 s at  $-160$  mV, 90 s at  $-220$  mV, 45 s at  $-280$  mV, and 19 s at  $-340$  mV.

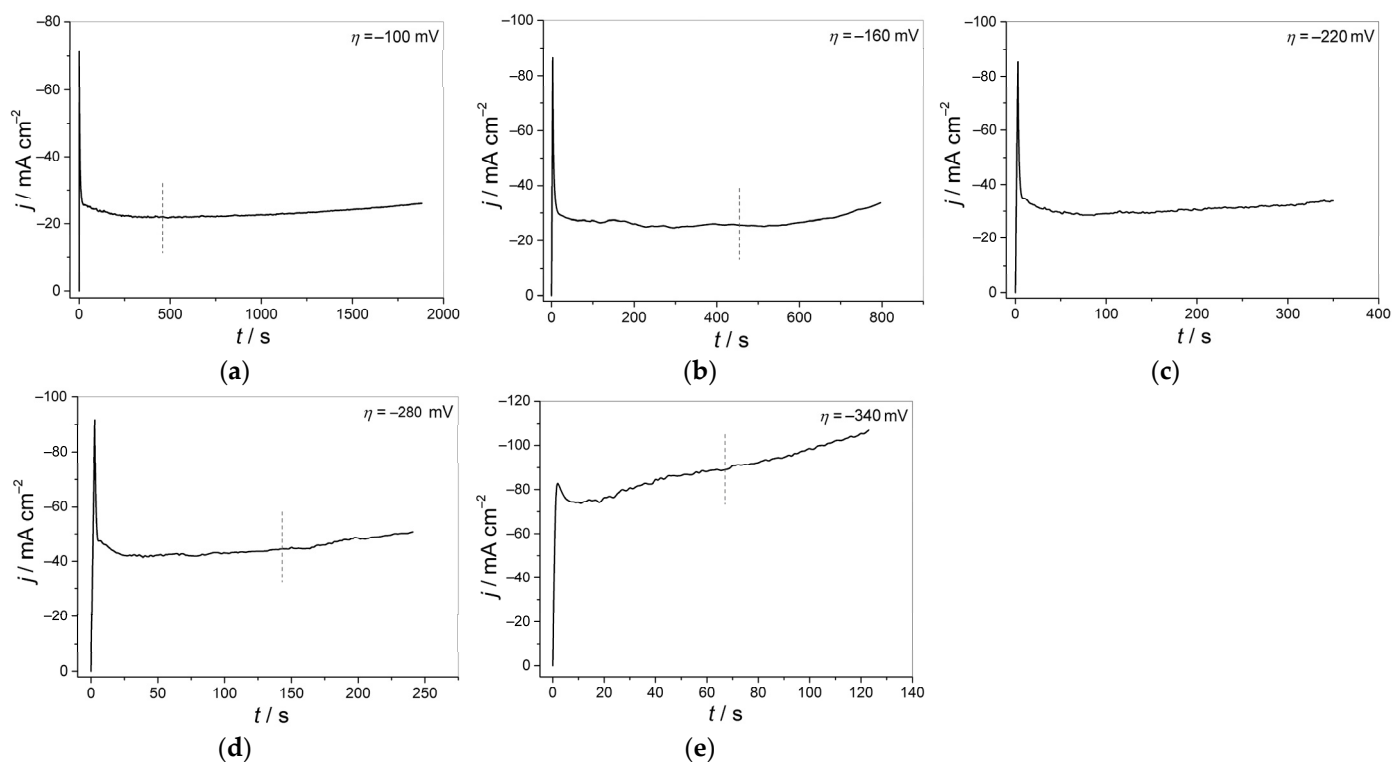


**Figure 2.** The chronoamperometric dependencies recorded from 0.35 M ZnO in 6.0 M KOH at overpotentials,  $\eta$ , of (a)  $-100$  mV; (b)  $-160$  mV; (c)  $-220$  mV; (d)  $-280$  mV; and (e)  $-340$  mV. The vertical dashed lines in (a,b) correspond to an electrodeposited charge of 1.5 mAh, while those given in (d,e) correspond to an electrodeposited charge of 0.75 mAh.

### 3.2. Morphological Analysis of Zn Irregular Forms

The morphology of the zinc deposit obtained at an overpotential of  $-100$  mV, belonging to the very beginning of the plateau of the limiting diffusion current density with an electrodeposited charge of 1.5 mAh, is shown in Figure 3. This electrodeposited charge is denoted by a vertical dashed line in Figure 2a, from which can be seen that the time that corresponded to it was below the critical value for initiation of dendritic growth. As supposed, dendrites were not formed under these electrolysis conditions. Instead of dendrites, grains of both irregular and regular shapes with well-defined crystal planes were formed (Figure 3 and Figure S1 in Supplementary Materials). Some of the grains had regular hexagonal shapes.

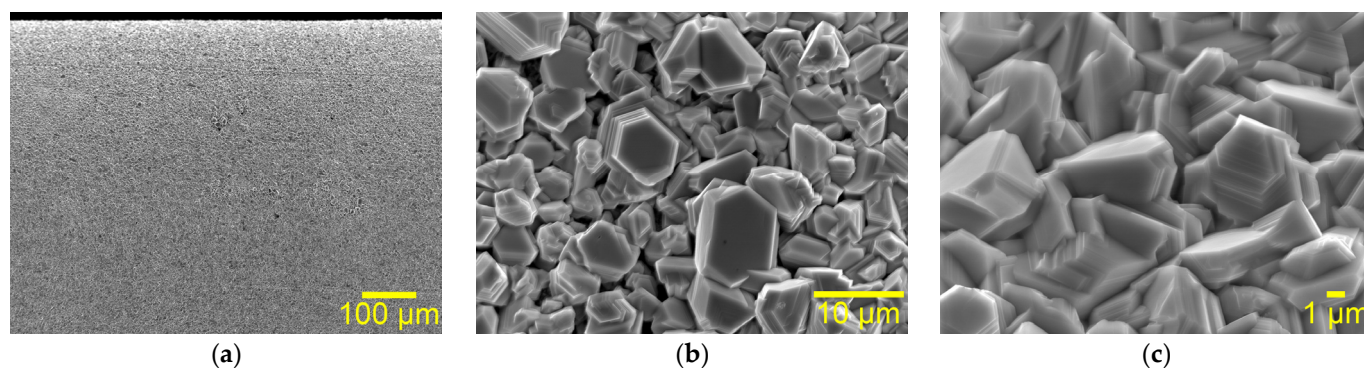


**Figure 3.** Morphologies of Zn deposit obtained from 0.35 M ZnO in 6.0 M KOH at an overpotential of  $-100$  mV with an electrodeposited charge of 1.5 mAh: (a) top view and (b,c) details from figure under (a) recorded at the higher magnifications. The time of electrodeposition: 460 s.

The morphology of the Zn deposit electrodeposited at the same overpotential, but with an electrodeposited charge of 6.0 mAh, is shown in Figure 4. This electrodeposited charge corresponds to an electrolysis time of 1880 s, which was above the critical value for initiation of dendritic growth (Figure 2a). Electrodeposition with this electrodeposited charge led to a formation of irregular forms with dendritic character (Figure 4a,b). Some of the typical forms of dendritic character are also given in the Supplementary Materials (see Figure S2). These forms do not follow the classical definition of a dendrite given by Wranglen [7], and they can be denoted as precursors of dendrites. Aside from them, both irregular and regular grains were also formed (Figure 4c).

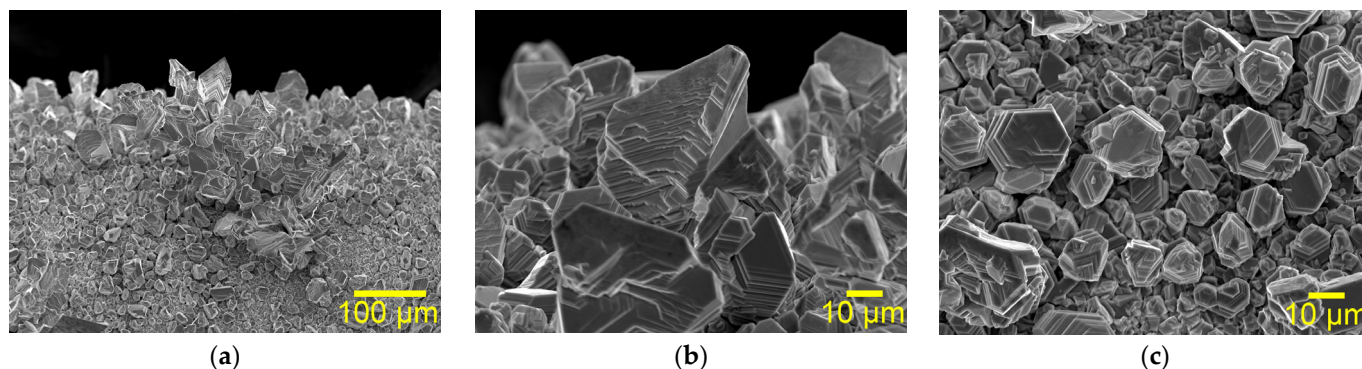


**Figure 4.** Morphologies of Zn deposit obtained from 0.35 M ZnO in 6.0 M KOH at an overpotential of  $-100$  mV with an electrodeposited charge of 6.0 mAh: (a) top view and (b,c) details from figure under (a) recorded at the higher magnifications. The time of electrodeposition: 1880 s.

Figure 5 shows the morphology of the Zn deposit obtained at an overpotential of  $-160$  mV with an electrodeposited charge of 1.5 mAh. The time corresponding to this electrodeposited charge is denoted by the vertical dashed line in Figure 2b and was below the critical value for an initiation of dendritic growth. Similar to the electrodeposition process at  $-100$  mV, grains of both irregular and regular shapes with well-defined crystal planes were formed with this electrodeposited charge (Figure 5a–c). Some of the grains also have regular hexagonal shapes (Figure 5b). Electrodeposition with this electrodeposited charge led to the appearance of the irregular forms of dendritic character, too (Figure 5c). More grains of regular and irregular shapes are shown in Figure S3 in Supplementary Materials.

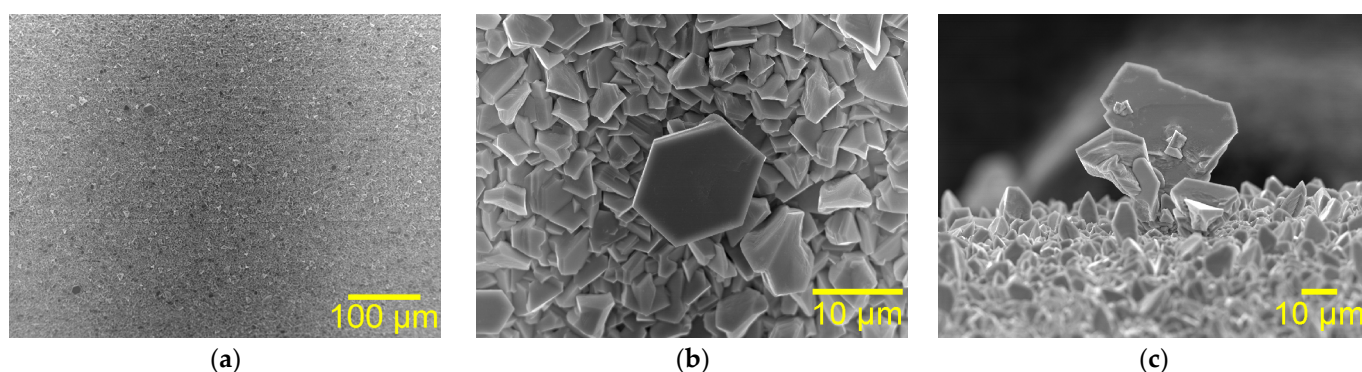


**Figure 5.** Morphologies of Zn deposit obtained from 0.35 M ZnO in 6.0 M KOH at an overpotential of  $-160$  mV with an electrodeposited charge of 1.5 mAh: (a) top view and (b,c) details from figure under (a) recorded at the higher magnifications. The time of electrodeposition: 452 s.

The morphology of the Zn deposit electrodeposited at the same overpotential, but with an electrodeposited charge of 3.0 mAh, is shown in Figure 6. This electrodeposited charge corresponds to an electrolysis time of 800 s, which was above the critical value for initiation of dendritic growth (Figure 2b). After 800 s the current density was 30.5% larger

than that after 550 s, which corresponds to the initiation of dendritic growth. Both irregular (Figure 6a,b) and regular (Figure 6c) dendrites oriented by the tips towards the bulk of the electrolyte were formed with this electrodeposited charge. It is worth noting that regular dendrites had compact, massive shapes. Some forms of irregular and regular dendrites are also shown in Figure S4 in Supplementary Materials.

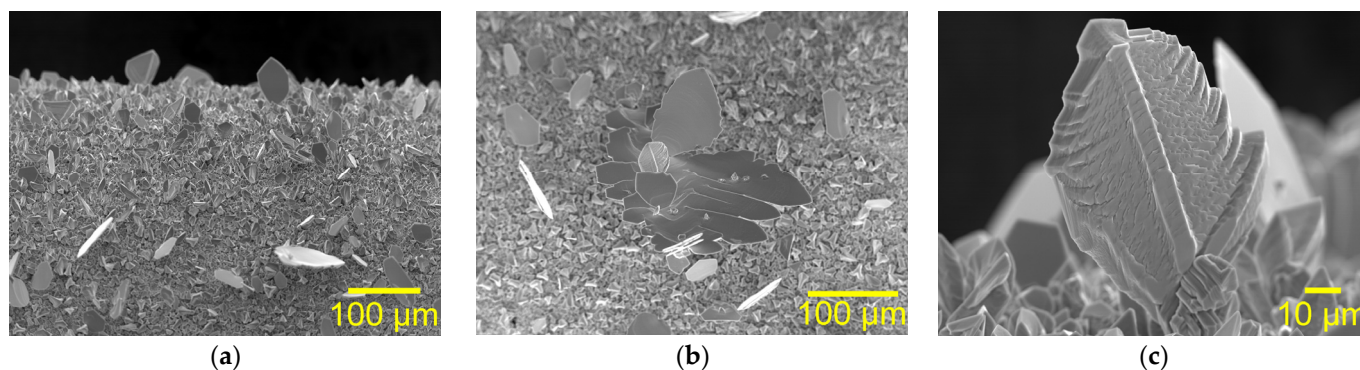


**Figure 6.** Morphologies of Zn deposit obtained from 0.35 M ZnO in 6.0 M KOH at an overpotential of  $-160$  mV with an electrodeposited charge of 3.0 mAh: (a) top view and (b,c) details from figure under (a) recorded at the higher magnifications. The time of electrodeposition: 800 s.

The mixture of branchy 2D (two-dimensional) and 3D (three-dimensional) dendrites was formed at an overpotential of  $-220$  mV with an electrodeposited charge of 1.5 mAh (Figures 7a and S5a). Formation of the dendrites with this electrodeposited charge was expected since the electrolysis time that corresponded to it was above the critical value for an initiation of dendritic growth (Figure 2c). Both 2D (Figure 7a,b) and 3D (Figure 7a,c) dendrites were oriented by the tips towards the bulk of the electrolyte, causing a considerable increase of the electrode surface during the duration of the electrolysis process.

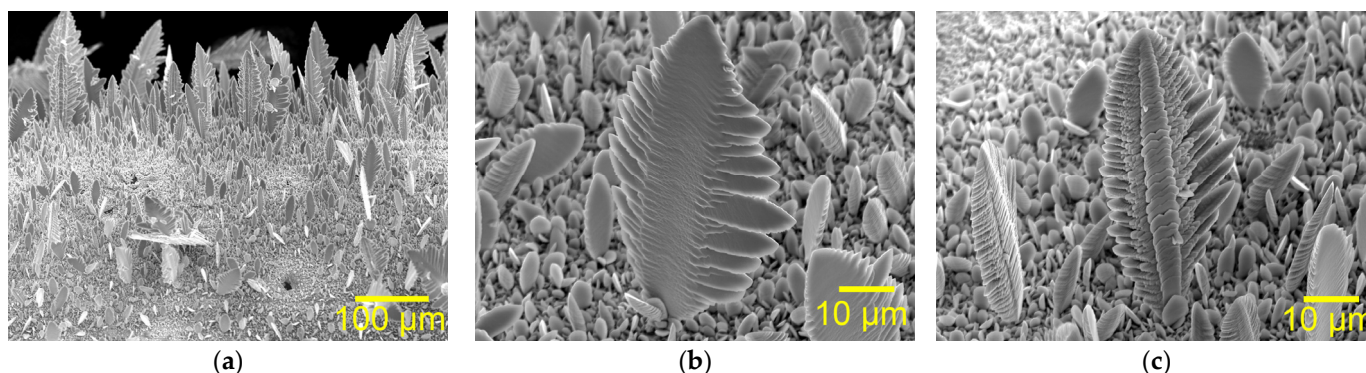


**Figure 7.** Morphologies of Zn deposit obtained from 0.35 M ZnO in 6.0 M KOH at an overpotential of  $-220$  mV with an electrodeposited charge of 1.5 mAh: (a) top view and (b,c) the types of dendrites. The time of electrodeposition: 350 s.

The similar shapes of the dendrites to those obtained at an overpotential of  $-220$  mV were also formed at overpotentials of  $-280$  mV (Figure 8) and  $-340$  mV (Figure 9) with the same electrodeposited charge. The mixture of branched 2D (Figures 8a,b, 9a,b and S5b,c) and 3D (Figures 8a,c, 9a,c and S5b,c) dendrites oriented by the tips towards the bulk of the electrolyte was formed at  $-280$  and  $-340$  mV. As expected, due to the larger applied overpotential of the electrodeposition, a larger number of the dendrites was formed at overpotentials of  $-280$  and  $-340$  mV than at  $-220$  mV.

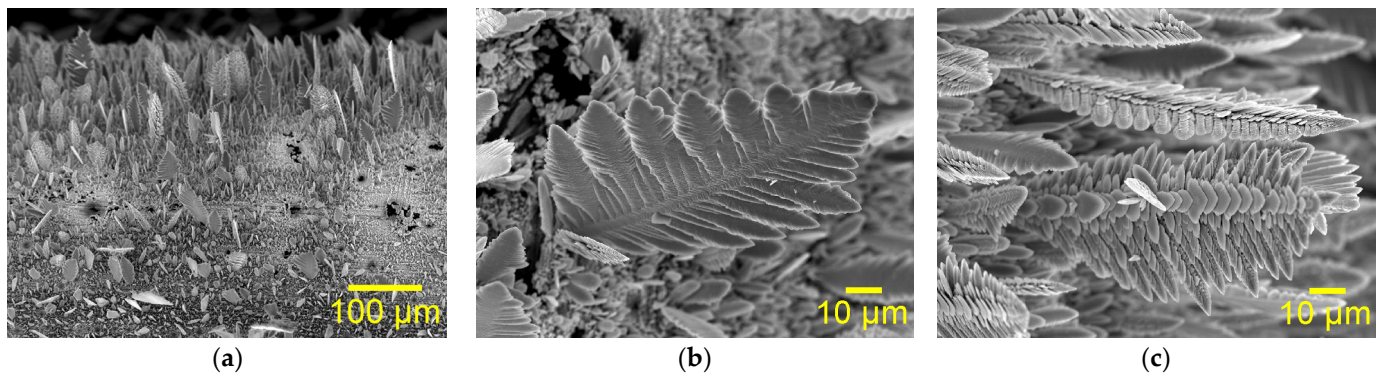


**Figure 8.** Morphologies of Zn deposit obtained from 0.35 M ZnO in 6.0 M KOH at an overpotential of  $-280$  mV with an electrodeposited charge of 1.5 mAh: (a) top view and (b,c) the types of dendrites. The time of electrodeposition: 242 s.

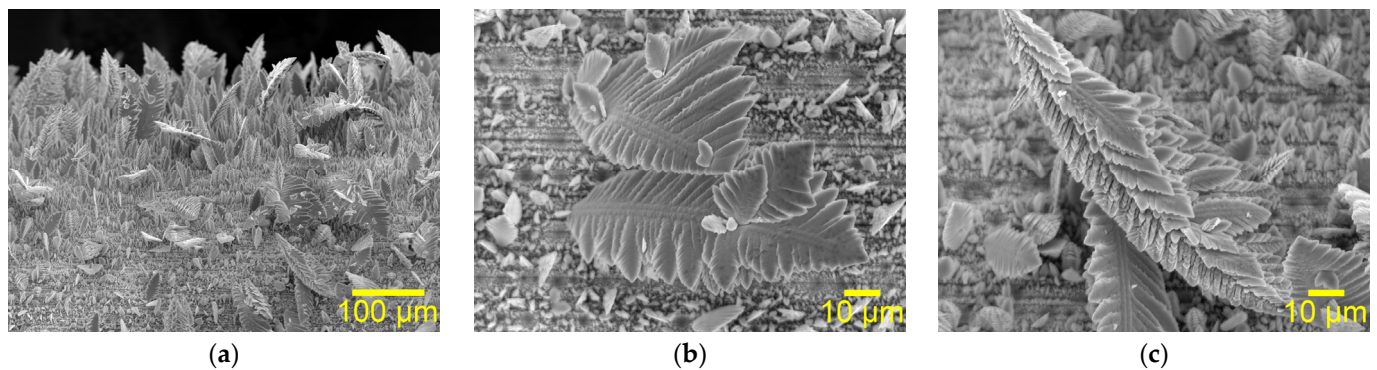


**Figure 9.** Morphologies of Zn deposit obtained from 0.35 M ZnO in 6.0 M KOH at an overpotential of  $-340$  mV with an electrodeposited charge of 1.5 mAh: (a) top view and (b,c) the types of dendrites. The time of electrodeposition: 123 s.

### 3.3. The Crystal Structure of Zn Dendritic Particles

The XRD (X-ray diffraction) patterns of Zn dendritic particles electrodeposited at overpotentials of  $-100$ ,  $-160$ ,  $-220$ ,  $-280$ , and  $-340$  mV are presented in Figure 10a–e, respectively. The Joint Committee on Powder Diffraction Standard (JCPDS number 00-04-0831) for Zn powder established for spherical distributed grains is shown in Figure 10f. The sharp diffraction peaks observed at  $2\theta$  angles of  $36.30^\circ$ ,  $39.0^\circ$ ,  $43.23^\circ$ ,  $54.33^\circ$ ,  $70.05^\circ$ , and  $70.66^\circ$  corresponded to (002), (100), (101), (102), (103), and (110) crystal planes of Zn, simultaneously confirming the electrocrystallization of Zn in the hexagonal closed pack type of crystal lattice [42]. It is worth noting that no other diffraction peaks were observed, pointing out a high purity of synthesized Zn particles.

At first glance, it can be seen that Zn crystallites in the precursors of dendrites formed at  $-100$  mV were oriented in larger extent in the (101) and (002) crystal planes (Figure 10a), while those in the dendrites produced at  $-160$ ,  $-220$ ,  $-280$ , and  $-340$  mV were predominantly oriented in the (002) crystal plane (Figure 10b–e). Simultaneously, all diffractograms strongly differed from the JCPDS standard for Zn. This difference represented a good indicator for the existence of preferred orientation in potentiostatically produced Zn particles. To establish it, the preferred orientation of Zn particles was estimated by applying a methodology based on a determination of “Texture Coefficients” (TCs(hkl)) and “Relative Texture Coefficients” (RTCs(hkl)) [8,43]. The values of TCs(hkl) coefficients larger than 1 point out the existence of the preferred orientation, while the values of RTCs(hkl) coefficients are dependent on the number of recorded diffraction peaks [8,40,43]. In our case, six main Zn diffraction peaks were recorded, and then the values of RTCs(hkl) coefficients larger than 16.7% pointed out the existence of the preferred orientation. The basis

of this methodology, together with relative intensities of the diffraction peaks, is given in Supplementary Materials, while the values of  $TCs(hkl)$  and  $RTCs(hkl)$  coefficients are given in Tables 1 and S1 for the particles produced at overpotentials belonging to the plateau of the limiting diffusion current density ( $-100$  mV and  $-160$  mV) and Tables 2 and S1 for the particles obtained at overpotentials outside the plateau of the limiting diffusion current density ( $-220$  mV,  $-280$  mV, and  $-340$  mV).

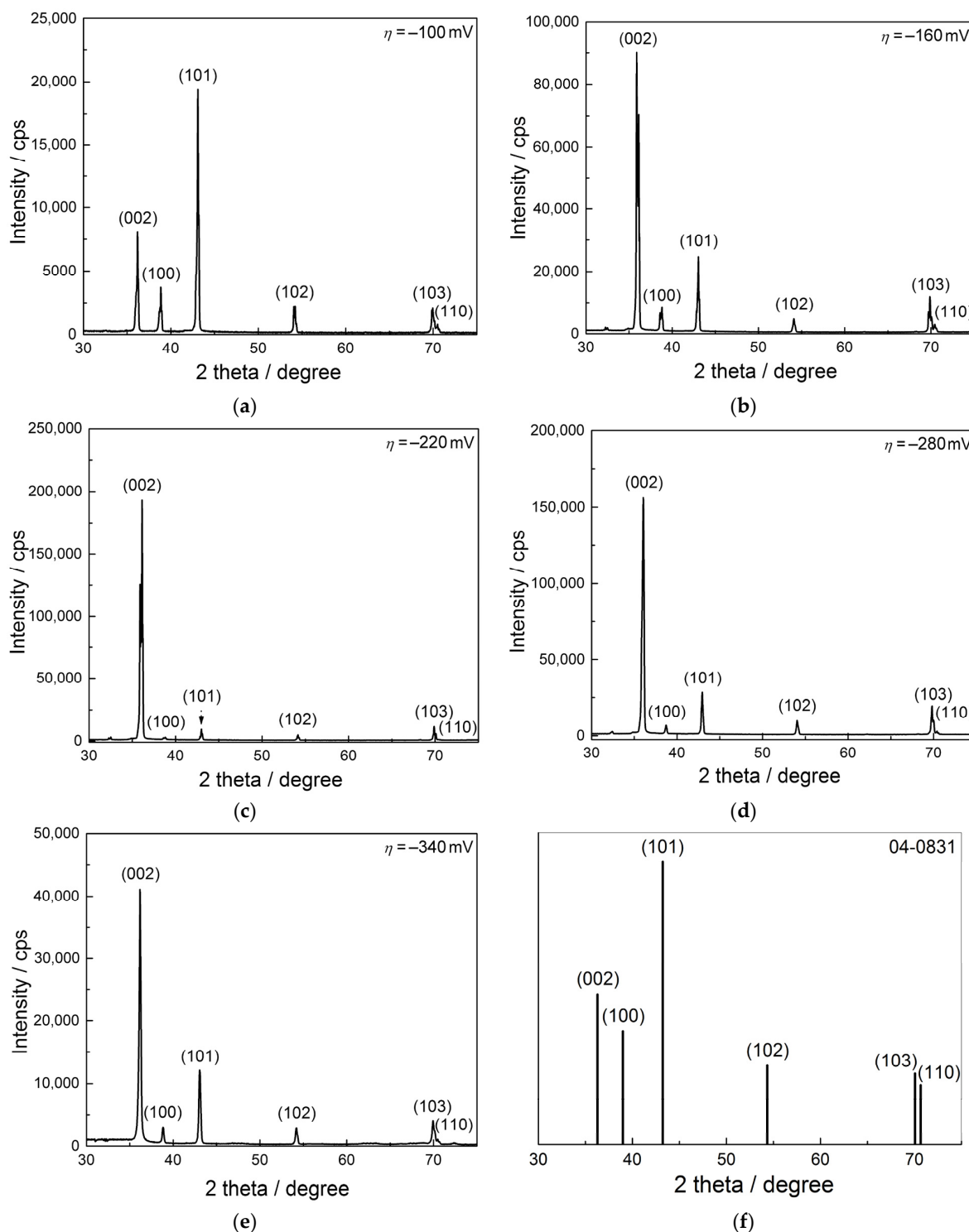


**Figure 10.** X-ray diffraction (XRD) patterns obtained for Zn particles electrodeposited from 0.35 M ZnO in 6.0 M KOH at overpotentials,  $\eta$ , of (a)  $-100$  mV; (b)  $-160$  mV; (c)  $-220$  mV; (d)  $-280$  mV; (e)  $-340$  mV; and (f) Zn standard (04-0831).

**Table 1.** The values of  $TCs(hkl)$  and  $RTCs(hkl)$  coefficients for Zn particles produced at overpotentials,  $\eta$ , of  $-100$  and  $-160$  mV.

Crystal Plane	$\eta = -100$ mV		$\eta = -160$ mV	
	$TCs(hkl)$	$RTCs(hkl)/\%$	$TCs(hkl)$	$RTCs(hkl)/\%$
(002)	1.1	23.7	3.1	55.5
(100)	0.67	14.4	0.39	7.0
(101)	1.4	30.1	0.45	8.0
(102)	0.59	12.7	0.31	5.5
(103)	0.62	13.3	0.87	15.6
(110)	0.27	5.8	0.47	8.4

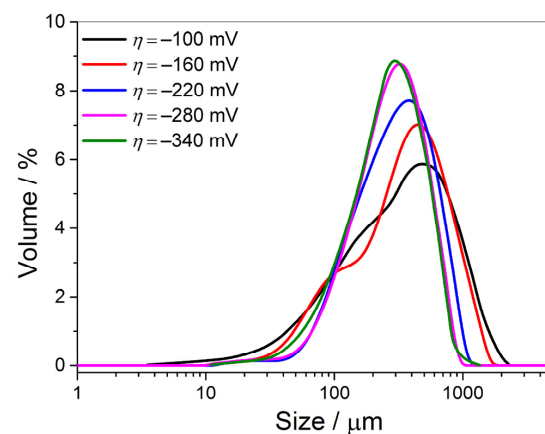
**Table 2.** The values of  $TCs(hkl)$  and  $RTCs(hkl)$  coefficients for Zn particles produced at overpotentials,  $\eta$ , of  $-220$ ,  $-280$ , and  $-340$  mV.

Crystal Plane	$\eta = -220$ mV		$\eta = -280$ mV		$\eta = -340$ mV	
	$TCs(hkl)$	$RTCs(hkl)/\%$	$TCs(hkl)$	$RTCs(hkl)/\%$	$TCs(hkl)$	$RTCs(hkl)/\%$
(002)	4.3	77.4	3.5	62.9	3.2	60.5
(100)	0.087	1.6	0.21	3.8	0.26	4.9
(101)	0.11	2.0	0.34	6.1	0.50	9.5
(102)	0.20	3.6	0.42	7.6	0.44	8.3
(103)	0.54	9.7	0.93	16.7	0.67	12.7
(110)	0.32	5.7	0.16	2.9	0.22	4.1

Analysis of data collected in Tables 1 and 2 pointed out that precursors of dendrites produced at  $-100$  mV showed (101)(002) preferred orientation, while dendrites of various shapes produced at  $-160$ ,  $-220$ ,  $-280$ , and  $-340$  mV exhibited the strong (002) preferred orientation.

### 3.4. The Dependence of Size of Zn Dendritic Particles on Applied Overpotential of the Electrodeposition

The effect of electrodeposition overpotential on the size of the dendritic particles is examined by particle size distribution (PSD) analysis of the particles obtained at various overpotentials with the same electrodeposited charge. The PSD dependencies obtained for the particles synthesized at the given overpotentials are shown in Figure 11, from which it can be seen that the particle size decreased with increasing the overpotential of electrodeposition. The uniform distribution was obtained for the dendrites synthesized at overpotentials of  $-220$ ,  $-280$ , and  $-340$  mV, while non-uniform distribution was obtained for the particles electrodeposited at overpotentials of  $-100$  and  $-160$  mV.

**Figure 11.** Particle size distribution (PSD) of Zn electrodeposited at overpotentials of  $-100$ ,  $-160$ ,  $-220$ ,  $-280$ , and  $-340$  mV.

#### 4. Discussion

The dendrites were the main morphological shapes formed by Zn electrolysis from the alkaline electrolyte. The shape of the dendrites strongly depended on the applied overpotential of the electrolysis and changed from irregular and compact, massive ones formed at the overpotential within the plateau of the limiting diffusion current density to the branchy 2D and 3D dendrites formed at overpotentials outside the limiting diffusion current density plateau. The particles of irregular shape denoted as precursors of dendrites were formed at the very beginning of the plateau of the limiting diffusion current density. The dendrites are formed in the diffusion control of electrodeposition, and various models, such as the “pyramid” growth model based on spiral dislocation growth controlled by bulk diffusion [44], diffusion-limited aggregation and phase-field models [45,46], a quantitative phase-field model based on Marcus kinetics theory [47], etc., have been proposed to explain the formation and growth of Zn dendrites.

The general theory of disperse deposits formation [10,11,48] based on the Diggle, Despić, and Bockris theory [44] and later upgraded by investigations of Popov and Nikolić [48]. It is one of a well-established theory that successfully explains the formation and growth of dendrites in general. According to this theory, a dendrite originates from a protrusion or irregularity formed in an initial phase of electrolysis, around which the tip of the spherical diffusion layer is formed. The current density at the tip of a protrusion is larger than on the flat part of the electrode surface, causing the formation of a dendrite as the final morphological form in the growth process. The tip of protrusion grows under the activation control, while simultaneously, the electrolysis process on the flat part of the electrode surface occurs predominately under the full diffusion control [10,11,44,48]. Regarding the polarization curve shown in Figure 1, it is necessary to point out that the electrolysis process remains diffusion-controlled after the end of the limiting diffusion current density plateau, and that the fast increase of the current density with the further increase of overpotential is a result of the increase of the real electrode surface caused by the fast growth of dendrites.

The electrodeposited charge, i.e., the electrodeposition time, does not affect the morphology but only the size of dendrites. Figure 12 shows the morphologies of dendrites obtained at overpotentials of  $-280$  mV (Figure 12a–c) and  $-340$  mV (Figure 12d–f) with an electrodeposited charge of  $0.75$  mAh. This electrodeposited charge is denoted by a vertical dashed line in Figure 2d,e and was above the critical times for an initiation of dendritic growth at both overpotentials. Comparing the shapes of dendrites obtained at the same overpotentials with different electrodeposited charges (Figures 8 and 12a–c;  $-280$  mV) and (Figures 9 and 12d–f;  $-340$  mV), it can be seen that they are the same in shape but different in size. It can be explained by the fact that the real current density always remains constant during electrodeposition in a potentiostatic regime [41] as follows: the dendritic growth is initiated at some overpotential belonging to the plateau of the limiting diffusion current density, and this overpotential is denoted as critical overpotential for an initiation of dendritic growth [10,11]. However, the growth of dendrites does not commence instantly at a given overpotential but after a certain time corresponding to a time necessary for an initiation of dendritic growth. After this time, due to the growth of the dendrites, the cathode surface starts to increase, and it is manifested by the rise of the current density in chronoamperometry curves (Figure 2). This rise in the current density keeps the real current density constant during the whole electrodeposition process, keeping the shape of the dendrites simultaneously unchanged. The effect of the electrodeposited charge is shown for overpotentials of  $-280$  and  $-340$  mV, but it is also valid for other overpotentials.

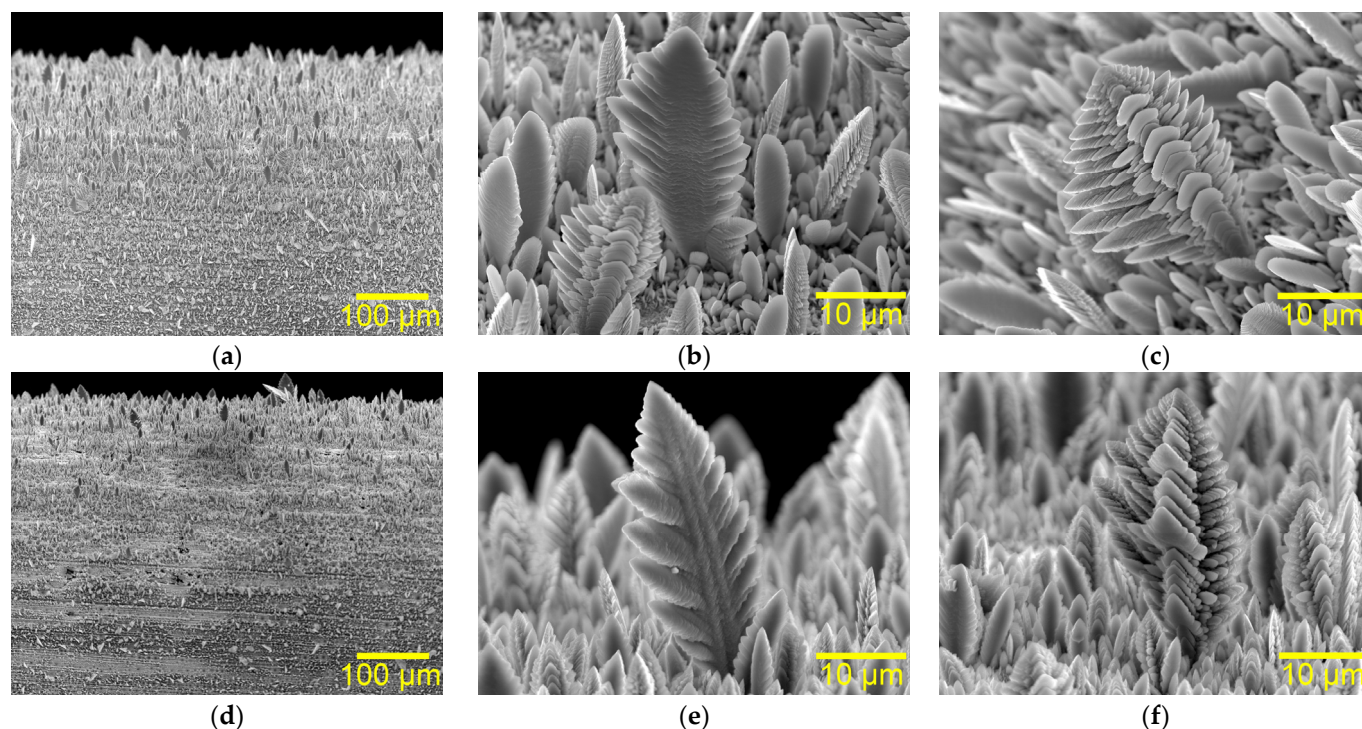


**Figure 12.** Morphologies of Zn deposits obtained from 0.35 M ZnO in 6.0 M KOH at overpotentials of (a–c)  $-280$  mV and (d–f)  $-340$  mV with an electrodeposited charge of 0.75 mAh. The time of electrodeposition: (a–c)  $-280$  mV: 143 s and (d–f)  $-340$  mV: 67 s.

Aside from the strong effect of the overpotential of electrodeposition on the shape of the dendritic particles, the applied overpotentials also affected their size (Figure 11). The dependence of the particle size on the overpotential of the electrodeposition can be explained as follows: The dependency of the nucleation rate,  $J$ , on the overpotential of the electrodeposition,  $\eta$ , is given by Equation (1) [10].

$$J = K_1 \exp\left(-\frac{K_2}{\eta^2}\right) \quad (1)$$

In Equation (1),  $K_1$  and  $K_2$  are constants independent of overpotential. Analysis of Equation (1) shows that the nucleation rate increases with the increase of the electrodeposition overpotential. It means that a larger number of nuclei, and hence, protrusions of which the dendrites are formed, arise at higher rather than at lower overpotentials. This will cause the formation of a larger number of dendrites in the growth process at higher than at lower overpotentials. Since the same electrodeposited charge is spent for the dendrite formation at all overpotentials, it is clear that it will form a larger number of smaller dendrites at higher than at lower overpotentials. The obtained PSD dependencies just confirmed this, since it is very clear from Figure 11 that the decrease in dendrite size occurs together with the increase in overpotential of the electrodeposition.

As already mentioned, the precursors of dendrites showed (101)(002) preferred orientation, while the dendrites showed a strong (002) preferred orientation. To explain the strong (002) preferred orientation, an analogy with lead electrolysis processes from the concentrated nitrate electrolyte was made. Pb and Zn belong to the same group of metals from an electrochemical point of view but to different types of crystal lattices. Regarding electrochemical parameters, they belong to a group of so-called normal metals, characterized by high exchange current density and overpotential for hydrogen evolution reaction and by low melting point values [49]. These parameters enable us to reach the diffusion control at relatively low overpotentials and to form powdered (disperse; irregular) deposits in a whole range of overpotentials [10]. On the other hand, Pb belongs to the face-centered

cubic type, while Zn belongs to the hexagonal close-packed type of crystal lattice. The irregular and the 2D dendritic forms having the strong (111) preferred orientation were formed during Pb electrolysis [8]. In a face-centered cubic lattice, the (111) crystal plane is a plane with the lowest surface energy. This plane survived a growth process during the duration of electrolysis as a slow-growing plane, constructing an interior, i.e., a body of dendrites. The other crystal planes, such as (220), (200), and (311), are fast-growing planes that disappear during the growth process. The tips, edges, and corners of dendrites were constructed from these crystal planes [50].

Similar to the face-centered cubic type of crystal lattice, each crystal plane in the hexagonal close-packed type of a crystal lattice also has a different arrangement of atoms [51]. In this type of crystal lattice, the (002) is a basal crystal plane with Zn atoms that are orderly arranged in a regular hexagon structure with a flat surface, where each atom of zinc is connected with nine surrounding atoms [51–55]. This arrangement of Zn atoms means that the (002) crystal plane has lower surface energy than all other crystal planes. Then, it is clear that this crystal plane is equivalent to the (111) crystal plane in the face-centered cubic crystal lattice of Pb. Hence, the (002) crystal plane represents a slow-growing plane, and as such, it remains during Zn electrolysis from the alkaline electrolyte, constructing the interior, i.e., body or stalk of Zn dendrites. It is confirmed by morphological analysis of the Zn dendrite electrodeposited at an overpotential of  $-160$  mV (Figure 13a). The regular hexagons formed inside the dendrite are identified, as seen in Figure 13b. Furthermore, the stacked hexagonal structures can easily be identified from Figure 13c, which presents the branches of the 3D dendrite. The other crystal planes, such as (100), (101), (102), (103), and (110), with higher surface energies and Zn atoms arranged in a more irregular wavy structure than the (002) crystal plane, can be denoted as the fast-growing crystal planes that disappear during the growth process, constructing tips, edges, and corners of the Zn dendrites. Simultaneously, it is clear that regular hexagons formed at overpotentials of  $-100$  and  $-160$  mV (Figures 3b, 4c and 5b) correspond to the (002) crystal plane.

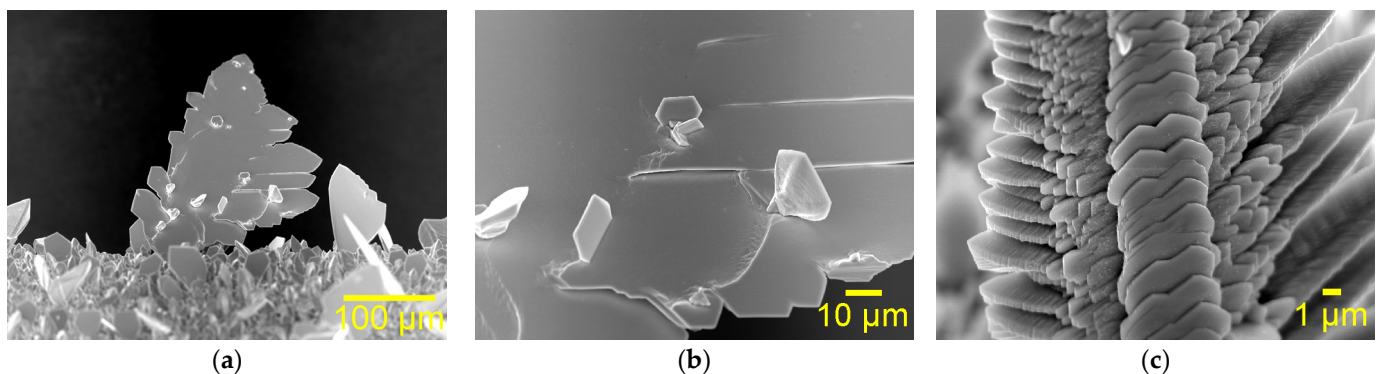


**Figure 13.** (a) Zn dendrite obtained from 0.35 M ZnO in 6.0 M KOH at an overpotential of  $-160$  mV with an electrodeposited charge of 1.5 mAh; (b) details from the dendrite shown in figure under (a); and (c) the branches of 3D dendrites electrodeposited at an overpotential of  $-220$  mV with an electrodeposited charge of 1.5 mAh (a detail from the dendrite shown in Figure 7c).

The strong correlation between the morphology of dendrites and the preferred orientation in the crystal plane with the lowest surface energy can be confirmed by the analysis of tin electrodeposition processes. Sn belongs to the same group of metals from an electrochemical point of view as Pb and Zn (the group of so-called normal metals) but to a different type of crystal lattice, i.e., to the body-centered tetragonal type. The electrolytically produced dendrites of Sn from the alkaline electrolyte exhibited the strong (220)(440) preferred orientation, which are the crystal planes with the lowest surface energy for this type of crystal lattice [40]. Hence, the electrochemical parameters prevail over those belonging to the determined type of crystal lattice.

The high purity of the produced dendritic particles can also be attributed to the predominant orientation of Zn crystallites in the (002) crystal plane. As the crystal plane with the lowest surface energy, the (002) crystal plane has more stable thermodynamic properties than all other crystal planes, making this plane electrochemically less active than the other crystal planes [51,55]. This causes the Zn particles with this predominant preferred orientation to have better corrosion resistance than those with other preferred orientations.

## 5. Conclusions

Morphological and structural analysis of zinc dendritic particles was performed to establish a correlation between these two characteristics of particles. The dendrites of Zn were produced potentiostatically from the alkaline electrolyte at overpotential, which belonged to the plateau of the limiting diffusion current density ( $-160$  mV), as well as at those outside the plateau in the zone of the fast growth of the current density with increasing the overpotential ( $-220$  mV,  $-280$  mV, and  $-340$  mV). The particles of irregular shape with dendritic character denoted as precursors of dendrites were formed at the very beginning of the plateau of the limiting diffusion current density ( $-100$  mV). The concentrations of  $0.35$  M ZnO and  $6.0$  M KOH were in the range of values typically used in the secondary Zn–air batteries. The obtained particles were characterized by scanning electron microscope (SEM; morphology) and X-ray diffraction (XRD; crystal structure), while the dependency of the particle size on the electrolysis overpotential was estimated by the particle size distribution (PSD) analysis.

On the basis of the results of performed analyses, it can be concluded that the shape of dendrites strongly depended on the applied overpotential of electrolysis. The two types of dendrites were identified by electrolysis from the alkaline electrolyte: (a) irregular and compact massive dendrites formed at the overpotential inside the plateau of the limiting diffusion current density, and (b) very branchy, both 2D (two-dimensional) and 3D (three-dimensional) dendrites formed at overpotentials outside the plateau of the limiting diffusion current density. Irregular and regular grains with well-defined crystal planes, including those hexagonal shapes, were concurrently formed beside dendrites at the overpotentials that belonged to the limiting diffusion current density plateau. The electrodeposited charge had only an influence on the size of dendrites, not on their shape. Simultaneously, the size of Zn dendritic particles decreased, while their uniformity increased with the increase of the overpotential of the electrolysis.

All types of dendrites showed a strong (002) preferred orientation, while precursors of the dendrites had (101)(002) preferred orientation. The strong (002) preferred orientation is explained by making an analogy with processes of lead electrolysis from the concentrated electrolyte. Pb and Zn belong to the same group of metals from the electrochemical point of view (so-called normal metals) and to various types of crystal lattice (Pb-face-centered cubic type and Zn-hexagonal close-packed type). The (002) crystal plane, as a plane with the lowest surface energy, builds the body or stalk of Zn dendrites, while tips, edges, and corners of the Zn dendrites are constructed from Zn crystallites oriented in other crystal planes.

**Supplementary Materials:** The following supporting information can be downloaded at: <https://www.mdpi.com/article/10.3390/met14121468/s1>. Figure S1: Zn grains of various shape obtained by the electrodeposition from  $0.35$  M ZnO in  $6.0$  M KOH at an overpotential of  $-100$  mV with an electrodeposited charge of  $1.5$  mAh; Figure S2: Various forms of dendritic character obtained by the electrodeposition from  $0.35$  M ZnO in  $6.0$  M KOH at an overpotential of  $-100$  mV with an electrodeposited charge of  $6.0$  mAh; Figure S3: Zn grains of irregular and regular shapes with well-defined crystal planes obtained by the electrodeposition from  $0.35$  M ZnO in  $6.0$  M KOH at an overpotential of  $-160$  mV with an electrodeposited charge of  $1.5$  mAh; Figure S4: Zn dendrites obtained by the electrodeposition from  $0.35$  M ZnO in  $6.0$  M KOH at an overpotential of  $-160$  mV with an electrodeposited charge of  $3.0$  mAh: (a) irregular shape, and (b) regular shape; Figure S5: The mixture of branchy 2D (two-dimensional) and 3D (three-dimensional) dendrites obtained by the electrodeposition from  $0.35$  M ZnO in  $6.0$  M KOH with an electrodeposited charge of  $1.5$  mAh

at overpotentials of: (a)  $-220$  mV, (b)  $-280$  mV, and (c)  $-340$  mV; Table S1: Texture calculations for Zn dendritic particles produced potentiostatically at overpotentials of  $-100$ ,  $-160$ ,  $-220$ ,  $-280$  and  $-340$  mV.  $R$ —Intensity of the diffraction peak;  $TC$ —Texture Coefficient;  $RTC$ —Relative Texture Coefficient;  $s$ —Zn standard.

**Author Contributions:** Conceptualization, N.D.N.; methodology, N.D.N.; validation, N.D.N., J.D.L., N.L.I., S.I.S., P.M.Ž. and V.M.M.; investigation, N.D.N., J.D.L., N.L.I., S.I.S., N.S.V. and V.M.M.; resources, N.D.N., N.L.I., N.S.V. and V.M.M.; writing—original draft preparation, N.D.N. and P.M.Ž.; writing—review and editing, N.D.N., J.D.L., N.L.I., S.I.S. and V.M.M.; visualization, N.D.N.; supervision, N.D.N.; project administration, N.D.N.; funding acquisition, N.D.N. All authors have read and agreed to the published version of the manuscript.

**Funding:** This research was funded by the Ministry of Science, Technological Development, and Innovation of the Republic of Serbia (Contract No. 451-03-66/2024-03/200026) and the Science Fund of RS (Grant No. AdCatFC: 7739802).

**Data Availability Statement:** The raw data supporting the conclusions of this article will be made available by the authors on request.

**Conflicts of Interest:** The authors declare no conflicts of interest.

## References

1. Pei, P.; Wang, K.; Ma, Z. Technologies for extending zinc–air battery’s cyclife: A review. *Appl. Energy* **2014**, *128*, 315–324. [[CrossRef](#)]
2. Zuo, Y.; Wang, K.; Pei, P.; Wei, M.; Liu, X.; Xiao, Y.; Zhang, P. Zinc dendrite growth and inhibition strategies. *Mater. Today Energy* **2021**, *20*, 100692. [[CrossRef](#)]
3. Zheng, X.; Ahmad, T.; Chen, W. Challenges and strategies on Zn electrodeposition for stable Zn-ion batteries. *Energy Storage Mater.* **2021**, *39*, 365–394. [[CrossRef](#)]
4. Minakshi, M.; Appadoo, D.; Martin, D.E. The Anodic Behavior of Planar and Porous Zinc Electrodes in Alkaline Electrolyte. *Electrochim. Solid-State Lett.* **2010**, *13*, A77–A80. [[CrossRef](#)]
5. Minakshi, M.; Ionescu, M. Anodic behavior of zinc in Zn-MnO<sub>2</sub> battery using ERDA technique. *Int. J. Hydrogen Energy* **2010**, *35*, 7618–7622. [[CrossRef](#)]
6. Rosen, J.; Hutchings, G.S.; Lu, Q.; Forest, R.V.; Moore, A.; Jiao, F. Electrodeposited Zn Dendrites with Enhanced CO Selectivity for Electrocatalytic CO<sub>2</sub> Reduction. *ACS Catal.* **2015**, *5*, 4586–4591. [[CrossRef](#)]
7. Wranglen, G. Dendrites and Growth Layers in the Electrocrystallization of Metals. *Electrochim. Acta* **1960**, *2*, 130–146. [[CrossRef](#)]
8. Nikolić, N.D.; Maksimović, V.M.; Avramović, L. Correlation of Morphology and Crystal Structure of Metal Powders Produced by Electrolysis Processes. *Metals* **2021**, *11*, 859. [[CrossRef](#)]
9. Fu, J.; Cano, Z.P.; Park, M.G.; Yu, A.; Fowler, M.; Chen, Z. Electrically Rechargeable Zinc–Air Batteries: Progress, Challenges, and Perspectives. *Adv. Mater.* **2017**, *29*, 1604685. [[CrossRef](#)] [[PubMed](#)]
10. Popov, K.I.; Djokić, S.S.; Nikolić, N.D.; Jović, V.D. *Morphology of Electrochemically and Chemically Deposited Metals*; Springer: New York, NY, USA, 2016; pp. 1–368.
11. Nikolić, N.D.; Živković, P.M.; Lović, J.D.; Branković, G. Application of the general theory of disperse deposits formation in an investigation of mechanism of zinc electrodeposition from the alkaline electrolytes. *J. Electroanal. Chem.* **2017**, *785*, 65–74. [[CrossRef](#)]
12. Nikitin, V.S.; Ostanina, T.N.; Rudoi, V.M.; Kuloshvili, T.S.; Darintseva, A.B. Features of Hydrogen Evolution during Electrodeposition of Loose Deposits of Copper, Nickel and Zinc. *J. Electroanal. Chem.* **2020**, *870*, 114230. [[CrossRef](#)]
13. Ostanina, T.N.; Rudoi, V.M.; Nikitin, V.S.; Darintseva, A.B.; Demakov, S.L. Change in the physical characteristics of the dendritic zinc deposits in the stationary and pulsating electrolysis. *J. Electroanal. Chem.* **2017**, *784*, 13–24. [[CrossRef](#)]
14. Ostanina, T.N.; Rudoi, V.M.; Patrushev, A.V.; Darintseva, A.B.; Farlenkov, A.S. Modelling the Dynamic Growth of Copper and Zinc Dendritic Deposits under the Galvanostatic Electrolysis Conditions. *J. Electroanal. Chem.* **2015**, *750*, 9–18. [[CrossRef](#)]
15. Wang, R.Y.; Kirk, D.W.; Zhang, G.X. Effects of deposition conditions on the morphology of zinc deposits from alkaline zincate solutions. *J. Electrochem. Soc.* **2006**, *153*, C357–C364. [[CrossRef](#)]
16. Banik, S.J.; Akolkar, R. Suppressing Dendritic Growth during Alkaline Zinc Electrodeposition using Polyethylenimine Additive. *Electrochim. Acta* **2015**, *179*, 475–481. [[CrossRef](#)]
17. Li, C.; Wang, L.; Zhang, J.; Zhang, D.; Du, J.; Yao, Y.; Hong, G. Roadmap on the protective strategies of zinc anodes in aqueous electrolyte. *Energy Storage Mater.* **2022**, *44*, 104–135. [[CrossRef](#)]
18. Jabbari, V.; Foroozan, T.; Shahbazian-Yassar, R. Dendritic Zn Deposition in Zinc-Metal Batteries and Mitigation Strategies. *Adv. Energy Sustain. Res.* **2021**, *2*, 2000082. [[CrossRef](#)]
19. Wang, C.; Li, J.; Zhou, Z.; Pan, Y.; Yu, Z.; Pei, Z.; Zhao, S.; Wei, L.; Chen, Y. Rechargeable zinc-air batteries with neutral electrolytes: Recent advances, challenges, and prospects. *Energy Chem.* **2021**, *3*, 100055. [[CrossRef](#)]

20. Thomas Goh, F.W.; Liu, Z.; Andy Hor, T.S.; Zhang, J.; Ge, X.; Zong, Y.; Yu, A.; Khoo, W. A Near-Neutral Chloride Electrolyte for Electrically Rechargeable Zinc-Air Batteries. *J. Electrochem. Soc.* **2014**, *161*, A2080. [[CrossRef](#)]
21. Bengoa, L.N.; Bruno, S.; Lazzarino, H.A.; Seré, P.R.; Egli, W.A. Study of dendritic growth of zinc crystals on the edges of steel sheet. *J. Appl. Electrochem.* **2014**, *44*, 1261–1269. [[CrossRef](#)]
22. Bengoa, L.N.; Seré, P.R.; Conconi, M.S.; Egli, W.A. Morphology and Texture of Zinc Deposits Formed at the Edge of a Rotating Washer Electrode. *J. Mater. Eng. Perform.* **2016**, *25*, 2936–2942. [[CrossRef](#)]
23. Bengoa, L.N.; Pary, P.; Seré, P.R.; Conconi, M.S.; Egli, W.A. Dendritic Zinc Growth in Acid Electrolyte: Effect of the pH. *J. Mater. Eng. Perform.* **2018**, *27*, 1103–1108. [[CrossRef](#)]
24. Desai, D.; Wei, X.; Steingart, D.A.; Banerjee, S. Electrodeposition of preferentially oriented zinc for flow-assisted alkaline batteries. *J. Power Sources* **2014**, *256*, 145–152. [[CrossRef](#)]
25. Dundálek, J.; Šnajdr, I.; Libánský, O.; Vrána, J.; Pcedič, J.; Mazúr, P.; Kosek, J. Zinc electrodeposition from flowing alkaline zincate solutions: Role of hydrogen evolution reaction. *J. Power Sources* **2017**, *372*, 221–226. [[CrossRef](#)]
26. Wang, K. Solutions for Dendrite Growth of Electrodeposited Zinc. *ACS Omega* **2020**, *5*, 10225–10227. [[CrossRef](#)]
27. Lu, W.; Xie, C.; Zhang, H.; Li, X. Inhibition of Zinc Dendrite Growth in Zinc-Based Batteries. *ChemSusChem* **2018**, *11*, 3996–4006. [[CrossRef](#)]
28. Hu, N.; Tao, J.; Tan, Y.; Song, H.; Huang, D.; Liu, P.; Chen, Z.; Yin, X.; Zhu, J.; Xu, J.; et al. Comprehensive Understanding of Steric-Hindrance Effect on the Trade-Off Between Zinc Ions Transfer and Reduction Kinetics to Enable Highly Reversible and Stable Zn Anodes. *Adv. Energy Mater.* **2024**, *14*, 2404018. [[CrossRef](#)]
29. Guo, W.; Tian, F.; Fu, D.; Cui, H.; Song, H.; Wang, C. High-Performance Aqueous Calcium Ion Batteries Enabled by Zn Metal Anodes with Stable Ion-Conducting Interphases. *Nano Lett.* **2024**, *24*, 12095–12101. [[CrossRef](#)]
30. Yang, Z.; Lv, C.; Li, W.; Wu, T.; Zhang, Q.; Tang, Y.; Shao, M.; Wang, H. Revealing the Two-Dimensional Surface Diffusion Mechanism for Zinc Dendrite Formation on Zinc Anode. *Small* **2021**, *18*, 2104148. [[CrossRef](#)]
31. Liu, Y.; Li, L.; Ji, X.; Cheng, S. Scientific Challenges and Improvement Strategies of Zn-Based Anodes for Aqueous Zn-Ion Batteries. *Chem. Rec.* **2022**, *22*, e202200114. [[CrossRef](#)]
32. Wang, X.; Sun, C.; Wu, Z.-S. Recent progress of dendrite-free stable zinc anodes for advanced zinc-based rechargeable batteries: Fundamentals, challenges, and perspectives. *SusMat* **2023**, *3*, 180–206. [[CrossRef](#)]
33. Du, W.; Zhang, Z.; Iacoviello, F.; Zhou, S.; Owen, R.E.; Jervis, R.; Brett, D.J.L.; Shearing, P.R. Observation of Zn Dendrite Growth via Operando Digital Microscopy and Time-Lapse Tomography. *ACS Appl. Mater. Interfaces* **2023**, *15*, 14196–14205. [[CrossRef](#)] [[PubMed](#)]
34. Li, Z.; Robertson, A.W. Electrolyte engineering strategies for regulation of the Zn metal anode in aqueous Zn-ion batteries. *Battery Energy* **2023**, *2*, 20220029. [[CrossRef](#)]
35. Liang, Y.; Qiu, M.; Sun, P.; Mai, W. Comprehensive Review of Electrolyte Modification Strategies for Stabilizing Zn Metal Anodes. *Adv. Funct. Mater.* **2023**, *33*, 2304878. [[CrossRef](#)]
36. Dai, H.; Sun, T.; Zhou, J.; Wang, J.; Chen, Z.; Zhang, G.; Sun, S. Unraveling chemical origins of dendrite formation in zinc-ion batteries via in situ/operando X-ray spectroscopy and imaging. *Nat. Commun.* **2024**, *15*, 8577. [[CrossRef](#)]
37. Hao, G.; Tian, X.; Chen, X.; Dong, Y.; Hao, C.; Li, C. Challenges and strategies for constructing stable zinc metal anodes in mild aqueous zinc-ion batteries. *Mater. Today Chem.* **2024**, *38*, 102059. [[CrossRef](#)]
38. He, C.; Gou, Q.; Hou, Y.; Wang, J.; You, X.; Yang, N.; Tian, L.; Xie, G.; Chen, Y. Growth and inhibition of zinc anode dendrites in Zn-air batteries: Model and experiment. *Chin. J. Chem. Eng.* **2024**, *67*, 268–281. [[CrossRef](#)]
39. Zhai, C.; Zhao, D.; He, Y.; Huang, H.; Chen, B.; Wang, X.; Guo, Z. Electrolyte Additive Strategies for Suppression of Zinc Dendrites in Aqueous Zinc-Ion Batteries. *Batteries* **2022**, *8*, 153. [[CrossRef](#)]
40. Nikolić, N.D.; Lović, J.D.; Maksimović, V.M.; Živković, P.M. Morphology and structure of electrolytically synthesized tin dendritic nanostructures. *Metals* **2022**, *12*, 1201. [[CrossRef](#)]
41. Popov, K.I.; Pavlović, M.G.; Maksimović, M.D.; Krstajić, S. The comparison of galvanostatic and potentiostatic copper powder deposition on platinum and aluminium electrodes. *J. Appl. Electrochem.* **1978**, *8*, 503–514. [[CrossRef](#)]
42. Xing, Z.; Huang, C.; Hu, Z. Advances and strategies in electrolyte regulation for aqueous zinc-based batteries. *Coord. Chem. Rev.* **2022**, *452*, 214299. [[CrossRef](#)]
43. Berube, L.P.; Esperance, G.L. A Quantitative Method of Determining of the Degree of Texture of Zinc Electrodeposits. *J. Electrochem. Soc.* **1989**, *136*, 2314–2315. [[CrossRef](#)]
44. Diggle, J.W.; Despic, A.R.; Bockris, J.O. Mechanism of dendritic electrocrystallization of zinc. *J. Electrochem. Soc.* **1969**, *116*, 1503–1514. [[CrossRef](#)]
45. Matsushita, M.; Sano, M.; Hayakawa, Y.; Honjo, H.; Sawada, Y. Fractal structures of zinc metal leaves grown by electrodeposition. *Phys. Rev. Lett.* **1984**, *53*, 286–289. [[CrossRef](#)]
46. Wheeler, A.A.; Murray, B.T.; Schaefer, R.J. Computation of dendrites using a phase field model. *Phys. D Nonlinear Phenom.* **1993**, *66*, 243–262. [[CrossRef](#)]
47. Cogswell, D.A. Quantitative phase-field modeling of dendritic electrodeposition. *Phys. Rev.* **2015**, *92*, 011301. [[CrossRef](#)]
48. Popov, K.I.; Nikolić, N.D. General Theory of Disperse Metal Electrodeposits Formation. In *Electrochemical Production of Metal Powders, Series: Modern Aspects of Electrochemistry*; Djokić, S.S., Ed.; Springer: New York, NY, USA, 2012; Volume 54, pp. 1–62.

49. Winand, R. Electrodeposition of Metals and Alloys—New Results and Perspectives. *Electrochim. Acta* **1994**, *39*, 1091–1105. [[CrossRef](#)]
50. Nikolić, N.D.; Maksimović, V.M.; Branković, G. Morphological and Crystallographic Characteristics of Electrodeposited Lead from the Concentrated Electrolyte. *RSC Adv.* **2013**, *3*, 7466–7471. [[CrossRef](#)]
51. Fu, H.; Xiong, L.; Han, W.; Wang, M.; Kim, Y.J.; Li, X.; Yang, W.; Liu, G. Highly active crystal planes-oriented texture for reversible high-performance Zn metal batteries. *Energy Storage Mater.* **2022**, *51*, 550–558. [[CrossRef](#)]
52. Wang, X.; Meng, J.P.; Lin, X.G.; Yang, Y.D.; Zhou, S.; Wang, Y.P.; Pan, A.Q. Stable zinc metal anodes with textured crystal faces and functional zinc compound coatings. *Adv. Funct. Mater.* **2021**, *31*, 2106114. [[CrossRef](#)]
53. Jia, X.X.; Liu, C.F.; Neale, Z.G.; Yang, J.H.; Cao, G.Z. Active materials for aqueous zinc ion batteries: Synthesis, crystal structure, morphology, and electrochemistry. *Chem. Rev.* **2020**, *120*, 7795–7866. [[CrossRef](#)] [[PubMed](#)]
54. Wu, S.; Hu, Z.; He, P.; Ren, L.; Huang, J.; Luo, J. Crystallographic engineering of Zn anodes for aqueous batteries. *eScience* **2023**, *3*, 100120. [[CrossRef](#)]
55. Zhou, M.; Guo, S.; Li, J.; Luo, X.; Liu, Z.; Zhang, T.; Cao, X.; Long, M.; Lu, B.; Pan, A.; et al. Surface-preferred crystal plane for a stable and reversible zinc anode. *Adv. Mater.* **2021**, *33*, 2100187. [[CrossRef](#)] [[PubMed](#)]

**Disclaimer/Publisher’s Note:** The statements, opinions and data contained in all publications are solely those of the individual author(s) and contributor(s) and not of MDPI and/or the editor(s). MDPI and/or the editor(s) disclaim responsibility for any injury to people or property resulting from any ideas, methods, instructions or products referred to in the content.